Gapless quantum spin liquid in the triangular system $Sr_3CuSb_2O_9$

S. Kundu,[1,*] Aga Shahee,[1] Atasi Chakraborty,[2] K. M. Ranjith,[3] B. Koo,[3] Jörg Sichelschmidt,[3] Mark T.F. Telling,[4] P. K. Biswas,[4] M. Baenitz,[3] I. Dasgupta,[2] Sumiran Pujari,[1] and A. V. Mahajan[1,†]

[1]*Department of Physics, Indian Institute of Technology Bombay, Powai, Mumbai 400076, India*
[2]*School of Physical Sciences, Indian Association for the Cultivation of Science, Jadavpur, Kolkata 700032, India*
[3]*Max Planck Institute for Chemical Physics of Solids, 01187 Dresden, Germany*
[4]*ISIS Pulsed Neutron and Muon Source, STFC Rutherford Appleton Laboratory, Harwell Campus, Didcot, Oxfordshire OX110QX, United Kingdom*

(Dated: January 24, 2022)

Abstract

We report gapless quantum spin liquid behavior in the layered triangular $Sr_3CuSb_2O_9$ (SCSO) system. X-ray diffraction shows superlattice reflections associated with atomic site ordering into triangular Cu planes well-separated by Sb planes. Muon spin relaxation (μSR) measurements show that the $S = \frac{1}{2}$ moments at the magnetically active Cu sites remain dynamic down to 65 mK in spite of a large antiferromagnetic exchange scale evidenced by a large Curie-Weiss temperature $\theta_{cw} \simeq -143$ K as extracted from the bulk susceptibility. Specific heat measurements also show no sign of long-range order down to 0.35 K. The magnetic specific heat (C_m) below 5 K reveals a $C_m = \gamma T + \alpha T^2$ behavior. The significant T^2 contribution to the magnetic specific heat invites a phenomenology in terms of the so-called Dirac spinon excitations with a linear dispersion. From the low-T specific heat data, we estimate the dominant exchange scale to be $\sim$ 36 K using a Dirac spin liquid ansatz which is not far from the values inferred from microscopic density functional theory calculations ($\sim$ 45 K) as well as high-temperature susceptibility analysis ($\sim$ 70 K). The linear specific heat coefficient is about 18 mJ/mol-K^2 which is somewhat larger than for typical Fermi liquids.

Introduction: The search for novel spin liquids has been driving the community of quantum magnetism ever since the proposal of Fazekas and Anderson [1]. It is now theorized that spin liquids come in various flavors, may have gapped or gapless excitations, may be topological or not [2]. Frustration disfavors magnetic order and is thus generically sought as a route to realizing spin liquids. Geometric frustration from the lattice composed of triangular motifs forms a key class in this search going back to the Fazekas-Anderson work for the triangular lattice [1]. While the $S = \frac{1}{2}$ uniform triangular lattice (with nearest-neighbor Heisenberg exchange J_1) has 120° long-range order [3–5] also supported by theory [6–10], the presence of further neighbor exchanges has been argued to enhance frustration and induce spin liquid behavior [11–13]. One candidate state for such a spin liquid has linearly dispersing low-energy excitations [14] and has been dubbed as a Dirac quantum spin liquid (QSL). They lead to a T^2-variation of the heat capacity in zero magnetic field, and an additional linear-in-T variation in the presence of a magnetic field. For $S = \frac{1}{2}$ triangular lattices, previously reported spin liquids [15–21] have not shown a T^2 behavior in the specific heat. Here we report on the finding of such a candidate Dirac QSL in the $Sr_3CuSb_2O_9$ (SCSO) triangular lattice system.

Taking inspiration from the triple perovskite $Ba_3CuSb_2O_9$ (of the form $A_3B_3X_9$) with a hexagonal lattice which has been inferred to be a $S = \frac{1}{2}$ QSL [22, 23], we considered the possibility of replacing the Ba^{2+} by the smaller Sr^{2+} ion resulting in chemical pressure and concomitant effects on the crystal structure and the magnetic ground state. Ref. [24] has reported on the dielectric properties of $Sr_3CuNb_2O_9$ while SCSO is largely unexplored. These triple perovskites crystallize in the tetragonal crystal system which is different from that of $Ba_3CuSb_2O_9$. Significantly different ionic sizes and charges of Sb^{5+} (0.60 Å) and Nb^{5+} (0.64 Å) compared to Cu^{2+} (0.73 Å) should favor atomic site ordering at the B-sites. This has also been seen in homologous compounds $Sr_3CaIr_2O_9$ [25] and $Sr_3CaRu_2O_9$ [26]). With 1:2 ordering at the B-site, the (111) planes (pertinent to the pseudo-cubic lattice) will have successive Cu planes with an edge-shared triangular geometry separated by two Sb/Nb planes (see Fig. 1 for a schematic). X-ray diffraction indeed shows superlattice peaks supporting this site ordering in SCSO.

Our experiments on SCSO have shown the following salient results: 1) The bulk susceptibility of SCSO shows no sign of long-range order (LRO) down to 1.8 K. It shows Curie-Weiss behavior with a Curie-Weiss temperature $\theta_{cw} \simeq$ -143 K. There is no bifurcation in the zero-field cooled (ZFC) and field cooled (FC) magnetization in low field either. 2) Zero-field muon spin relaxation (ZF-μSR) data reconfirm the absence of any magnetic ordering down to 65 mK. Longitudinal-field μSR (LF-μSR) data show that the moments remain dynamic down to very low temperatures. 3) Magnetic heat capacity data are also devoid of any indications of a phase transition down to 0.35 K. A $\gamma T + \alpha T^2$ form is seen in the low-T behavior.

An unequivocal presence of a T^2 contribution in the magnetic specific heat, in the absence of any evidence of magnetic order, naturally suggests a phenomenology in terms of a Dirac QSL. Density functional theory (DFT) calculations for the B-site ordered structure also support a model of SCSO as a triangular lattice quantum anti-

ferromagnet with small further-neighbor frustrating antiferromagnetic exchanges (in the (111) planes pertinent to the pseudo-cubic cell) for which a Dirac QSL has been predicted [11–13].

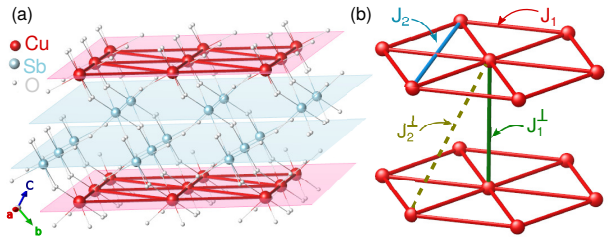

Figure 1: (a) A schematic of the SCSO crystal structure is shown highlighting the individual planes of Cu (red) and Sb (blue) atoms. The Sr atoms are omitted for visual clarity. (b) The paths corresponding to different exchange couplings.

Results and discussion: The Rietveld refinement of XRD data on our polycrystalline SCSO sample by Fullprof suite software [27] is shown in Fig. 2. Fitting with a body-centered tetragonal structure with space group $I4/mcm$ (140) (shown in SM [28]) does not account for a few peaks at low angles (region shown in the inset of Fig. 2). 1:2 atomic site ordering refines the data well with a propagation vector $\vec{K} = (\frac{1}{3}, \frac{1}{3}, \frac{1}{3})$. The obtained lattice parameters are $a = b = 5.547$ Å, $c = 8.248$ Å.

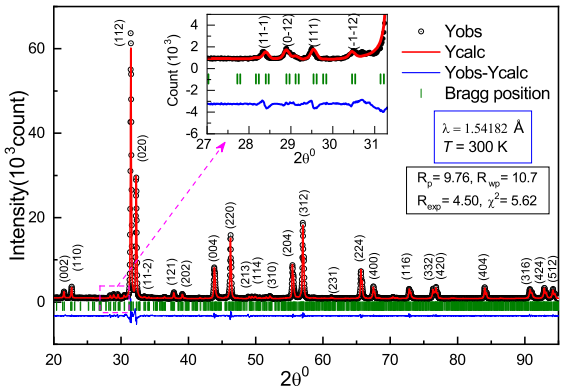

Figure 2: Rietveld refinement of $Sr_3CuSb_2O_9$ is shown along with Bragg positions and corresponding Miller indices (hkl) with K-modulation $(\frac{1}{3}, \frac{1}{3}, \frac{1}{3})$ (referred to a pseudo-cubic cell) to fit the superlattice peaks.

Fig. 3 shows the DC susceptibility, $\chi(T)$ $(=\frac{M(T)}{H})$ of SCSO in $H = 1$ kOe. No indications of long-range order are seen down to 2 K. We fit the data (in the high-temperature range of $150 - 300$ K) to the theoretical Triangular Lattice Antiferromagnet (TLAF) model for a 2D spin-1/2 system [29] using $\chi = \chi_0 + \chi_{\rm TLAF}$ as in Ref. [30, 31]. Here χ_0 is the temperature independent susceptibility (arising from core diamgnetism and a van Vleck contribution), $C = N_A g^2 \mu_B^2 / 4k_B$ is the Curie constant, and J_1 is the nearest neighbour exchange coupling [32]. Fixing $C = 0.375$ K cm^3/mol Cu for our $S = \frac{1}{2}$ system, this TLAF fit yields χ_0= -2.10× 10^{-4} cm^3/mol Cu, and $|J_1/k_B| = 70$ K [33].

The inset of Fig. 3 shows the ZFC/FC susceptibility. No bifurcation is seen down to 2 K. AC susceptibility data (see SM [28]) show no anomaly either. This rules out the existence of spin-glass behavior in the system [34].

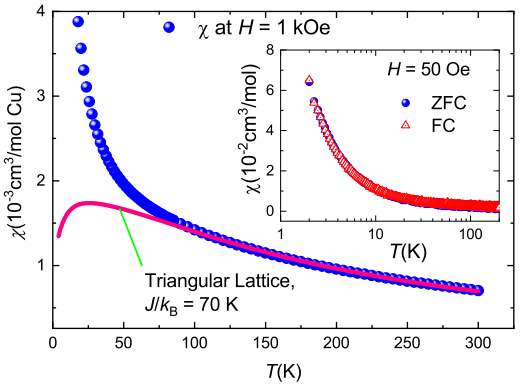

Figure 3: The variation of $\chi(T)$ for SCSO in $H = 1$ kOe is shown in the main figure. The solid line is a theoretical TLAF fit for data in the range 150-300 K and then extrapolated down to 2 K. In the inset, no bifurcation is seen in the plot of $\chi(T)$ vs T between ZFC and FC data in $H = 50$ Oe.

Additional evidence for the absence of static magnetism down to even lower temperatures (65 mK) was gathered from μSR experiments. The ZF muon asymmetry was measured as a function of T between 65 mK and 4 K. Strong relaxation of the muon is seen at the lowest temperature and we fit the time dependence of the asymmetry to $A(t) = A_0 G_{KT}(\Delta, t) e^{-\lambda(T)t} + A_{bg}$. Here, $G_{KT}(\Delta, t)$ is the static Kubo-Toyabe Gaussian function coming from relaxation due to the nuclear moments whereas the exponential decrease is from the relaxation due to electron moments. A_{bg} is the constant background signal (due to a small fraction of the muons missing the sample and hitting the sample holder and cryostat wall) and A_0 is the initial muon asymmetry. The muon asymmetry data at various T are shown in Fig. 4. The absence of oscillations in the muon asymmetry data suggests the absence of any short/long-range magnetic ordering down to 65 mK. Further, the absence of the 1/3rd tail suggests the dynamic nature of the electronic spins. The LF-μSR data will further validate the dynamic nature of the moments.

As seen in Fig. 4, the relaxation curves are essentially unchanged from 65 mK to about 1 K and at higher temperatures, the muon depolarisation rate decreases. From the above analysis, the muon relaxation rate due to electron moments is obtained as shown in the inset of Fig. 4. It is seen that there is a gradually faster relaxation of muons with a lowering of temperature. However, there is

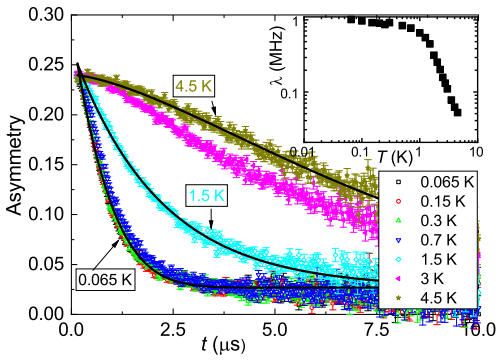

Figure 4: The variation of the muon asymmetry with time is shown at various temperatures in zero field for $Sr_3CuSb_2O_9$. On fitting these data as described in the text, the muon relaxation rate was obtained and is shown in the inset.

no large increase or a critical divergence and the electron moments remain dynamic till the lowest temperatures.

We have also monitored muon relaxation in longitudinal fields and find that even in our highest field of 3200 Oe, residual relaxation is still present (see SM [28]). The field dependence is remarkably similar to that of $YbMgGaO_4$ [35] with a local moment fluctuation frequency of about 18 MHz and the presence of long-time spin correlations. The qualitative and quantitative outcomes of μSR on SCSO are typical of other QSL.

To further rule out LRO and to probe the nature of low-energy excitations, we measured the heat capacity of the sample $C_{\rm p}(T)$ in different fields (0-90 kOe) in the T-range (0.35 - 200) K. As shown in Fig. 5, a hump is seen in the heat capacity which moves to higher temperatures with increasing field, and can be ascribed to the Schottky anomaly commonly seen in many quantum magnets [22, 36, 37]. This arises from a small fraction of free spins (either of extrinsic origin or from edge spins of correlated regions). In the low-T regime, the scaling is observed to be close to T^2. This already hints at the presence of linearly-dispersing excitations. We thus model the specific heat below 6 K as $C_{\rm p}(T,H) = \gamma(H)T + \alpha(H)T^2 + fC_{\rm Schottky}(T,H)$ motivated by a Dirac QSL phenomenology. $C_{\rm Schottky}$ is the standard Schottky contribution of a two-level system (see SM [28]) with f being the fraction of free $S = \frac{1}{2}$ entities. Solid lines in Fig. 5 show fits to the as-measured $C_{\rm p}$ with the parameter values $\gamma_{avg} = 18$ mJ/mol-K^2, $\alpha_{avg} = 15$ mJ/mol-K^3, and $f = 2.5\%$. For γ and α, the quoted average is over the fits for $H \geq 30$ kOe. The Schottky fraction f was obtained from the fit for 90 kOe data and kept fixed for other fields. A βT^3 contribution from the lattice can also be included in the analysis, but it makes no essential difference to the fits. Fits at high-T to the lattice heat capacity help us fix $\beta = 3 \times 10^{-4}$ J/mol-K^4 (see SM [28]). As the lattice contribution in the low-T range is negligible, we get very similar parameter values $\gamma_{avg} = 16$ mJ/mol-K^2, $\alpha_{avg} = 15$ mJ/mol-K^3 with $f = 2.5\%$. Most importantly, the fitting significantly worsens *without* a T^2 component and can not be considered as fitting the data (see SM [28]).

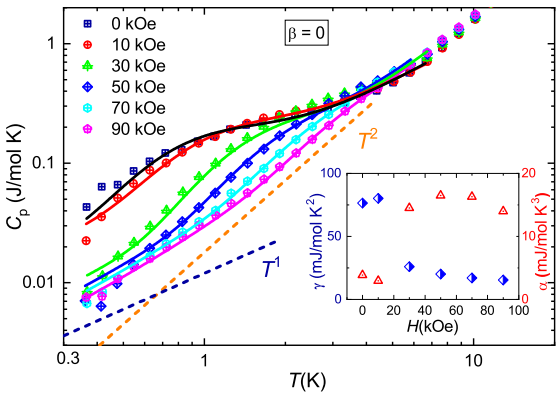

Figure 5: The heat capacity of SCSO is plotted as a function of temperature in various fields. The solid lines are fits as explained in the text. Dashed lines represent power law variations T^1 and T^2. Inset: The variation of the coefficients of the linear (blue diamonds; left y-axis) and quadratic (red triangles; right y-axis) terms is shown as a function of H.

As far as $S = \frac{1}{2}$ triangular lattice spin liquids are concerned, a linear variation of the low-temperature specific heat was observed in κ-(BEDT-TTF)$_2$Cu$_2$(CN)$_3$ [18] and $Ba_3CuSb_2O_9$ [22]. This was interpreted in terms of a spinon Fermi surface. However, the T^2 term in $C_{\rm m}(T)$ observed at low-T in SCSO is perhaps the first such observation in triangular $S = \frac{1}{2}$ magnets. From this crucial presence of T^2 contributions, we infer the presence of gapless excitations with a linear dispersion [38]. Within a Dirac QSL phenomenology that naturally gives such excitations, we can estimate the magnetic exchange strength from low-temperature specific heat data to compare with previous estimates from high-temperature data. We take the following effective mean-field Hamiltonian as our Dirac QSL ansatz $\mathcal{H} = \frac{J_{\rm eff}}{2} \sum_{\langle i,j\rangle \in \triangle \text{ lattice},\sigma} \chi_{ij} c^\dagger_{i,\sigma} c_{j,\sigma} +$ h.c. such that π-flux is inserted in the up triangles [13, 39]. $J_{\rm eff}$ is expected to be the same order as the dominant exchange ($J_{\rm eff} \sim \mathcal{O}(J_1)$) Near the single Dirac cone in the Brillouin zone (see SM [28] for details), the effective low energy spectrum is $\epsilon_{\mathbf{k}} = \pm\sqrt{\frac{3}{2}} J_{\rm eff}\, k$. Therefore at low temperatures ($T \to 0$), we obtain $\frac{C(T)}{k_B} = 2.292 \frac{(k_B T)^2}{J_{\rm eff}^2}$. In presence of Zeeman coupling to an external magnetic field, this gets modified to $\frac{C(T)}{k_B} \approx 2.292 \frac{(k_B T)^2}{J_{\rm eff}^2} + 0.696 \frac{(k_B T)\left(\frac{g\mu_B |H|}{2}\right)}{J_{\rm eff}^2}$ as $\frac{g\mu_B |H|}{2k_B T} \gg 1$, which is indeed the functional form used earlier for fits. From the coefficient α_{avg} of the T^2 contribution, we estimate $\frac{J_1}{k_B} \sim 36$ K. This completely independent low-T, macroscopic or thermodynamic estimate for J_1 is of the same order as the previous estimate from

high-T susceptibility data which we consider significant [40]. In fact, from the low field values of α, the estimate is $\frac{J_1}{k_B} \sim 76$ K. Furthermore, these estimates also agree with microscopic estimates based on a DFT study of the SCSO perovskite system to be discussed soon.

We finally note an anomaly that is present in the heat capacity data at low fields, seen as a "separation" between the curves as we go from 10 kOe to 30 kOe in Fig. 5. This is also reflected in the fits based on our linearly-dispersing Dirac QSL ansatz as a jump in α and γ at these fields as seen in the inset of Fig. 5. Note that the Schottky gap is non-zero even in the absence of a magnetic field for SCSO (see SM [28]) which is a feature seen in other QSLs as well [22, 36, 37] and is ascribed to interaction of the orphan spins with the correlated regions. We speculate this happens when the orphan spins suddenly decouple from the correlated regions as the applied field exceeds ~ 10 kOe (which might be the effective internal field strength of their interaction). Since this "separation" in the data sets at low field is observed in the raw or as-measured C_p data prior to any fitting, we think that it has a distinct physical origin (leading to an artificial jump in α, γ parameters when using a fitting form based on assuming only linear-dispersing excitations). There could be other explanations for this observation as well. Also for $H \geq 30$ kOe, a slight decrease of γ with field is found from the data whereas an increase is predicted by our ansatz, while α remains roughly independent of field as predicted by our ansatz. Nonetheless, another supporting feature in the data is that the ratio of the quadratic and linear components agrees with the theoretical value quite well for $H = 50$ kOe and to within a factor of 3 for all $H \geq 30$ kOe data sets despite the anomalous field dependence of γ. The deviations suggest that something else may also be contributing to the heat capacity in addition to the linearly dispersing excitations. We remark here that 1) $\frac{g\mu_B|H|}{2k_BT} \gg 1$ is not strictly true for the applied fields, and 2) that our ansatz is at a mean-field level, though the T^2 behavior is robust to beyond mean-field effects for a Dirac QSL. [41, 42]

To check the viability of a Dirac QSL phenomenology argued above as arising from a triangular quantum magnet with further-neighbor frustrating antiferromagnetic exchanges [11–13], we have carried out first principles electronic structure calculations based on DFT for the experimentally determined triple perovskite structure of $Sr_3CuSb_2O_9$. All the electronic structure calculations are carried out using DFT in the pseudo-potential plane-wave basis within the generalized gradient approximation (GGA) [43] supplemented with Hubbard U [44] as encoded in the Vienna *ab initio* simulation package (VASP) [45, 46] with projector augmented wave potentials [47, 48]. The calculations are done with standard values of $U_{\rm eff} \equiv U_{\rm d} - J_{\rm H} = 6.5$ eV [44] chosen for Cu. The non-spin-polarized total and Cu-d partial density of states (DOS) for SCSO (see SM [28]) reveal that the Fermi level is dominated by partially filled Cu e_g states. The oxygen $O-p$ states are completely occupied while Sb s and p states and Sr s states are completely empty consistent with the nominal ionic formula, $Sr_3^{2+}Cu^{2+}Sb_2^{5+}O_9^{2+}$ of this compound. Spin polarized calculations with ferromagnetic (FM) arrangement of Cu spins yields total moment 1.0 μ_B per formula unit, which further supports the $S = \frac{1}{2}$ moment of Cu and is consistent with the experimentally determined effective moment ($\mu_{\rm eff} = 1.72\mu_B$). However, the calculated magnetic moment per Cu site is 0.80 μ_B, while rest of the moment is hosted on the ligand sites due to substantial hybridization of Cu with ligands.

To estimate the exchange interactions, we consider the following Hamiltonian $H = J_1 \sum_{\langle i,j\rangle}^{\rm intra} \mathbf{S}_i.\mathbf{S}_j + J_2 \sum_{\langle\langle i,j\rangle\rangle}^{\rm intra} \mathbf{S}_i.\mathbf{S}_j + J_1^{\perp} \sum_{\langle i,j\rangle}^{\rm inter} \mathbf{S}_i.\mathbf{S}_j + J_2^{\perp} \sum_{\langle i,j\rangle}^{\rm inter} \mathbf{S}_i.\mathbf{S}_j$. Here J_1, J_2, $J_1^{\perp}$ and $J_2^{\perp}$ are respectively the nearest-neighbor (nn), the next-nearest-neighbor (nnn) intra-layer and (two distinct) inter-layer Heisenberg exchange parameters. We have calculated them employing the "Four State" method [49, 50]. This is based on a computation of the total energy of the system with collinear spin alignment, where the spin configuration on two chosen sites are modified while restricting rest of the spins to a base configuration. Our calculations reveal that the estimates of the exchange interactions change up to 15% depending on the chosen base configuration. We find $J_1 \sim 3.92$ meV ($J_1/k_B \sim 45$ K) to be the dominant antiferromagnetic exchange in this system. This microscopic estimate agrees well with the values extracted from the high-temperature susceptibility data and low-temperature specific heat data. $J_1^{\perp} \sim 0.21$ meV and $J_2^{\perp} \sim 0.11$ meV are found be sub-dominant and robustly antiferromagnetic, thus adding to the frustration. $J_2 \sim 0.05$ meV was even smaller, and its sign also depended on the chosen base configuration. This last estimate is at the edge of the accuracy of our DFT calculations (~ 0.05 meV). The strength of the further-neighbor exchanges are relatively much smaller because the Cu atoms are far apart, as well as the intermediate Sb atoms are smaller in size. Our first principles DFT results corroborates well with the experimental results, and lends credence to the scenario of spin liquid behavior induced by further-neighbor frustrating exchanges [11–13].

Summary: Our comprehensive set of data on SCSO show a 1:2 site ordering between Cu and Sb ions (giving rise to nearly isolated $S = \frac{1}{2}$ triangular planes) and a lack of LRO together with the presence of dynamic moments down to the lowest temperatures (65 mK, which is well below $\theta_{\rm cw}$= -143 K). In contrast to other Kagome or pyrochlore based QSL, here the magnetic heat capacity at low-T follows $C_{\rm m} = \gamma T + \alpha T^2$. The T^2 behavior of C_m evinces the presence of gapless excitations with a linear dispersion, and the dominant exchange ex-

tracted through such a phenomenology agrees quantitatively with those from high-temperature susceptibility data and DFT estimates. We believe that the presence of further-neighbor antiferromagnetic exchanges induces Dirac QSL behavior in the triangular lattice system of SCSO. Our work offers new material directions to explore in the field of QSLs. Further work to unravel the magnitude of the further-neighbor couplings or possibly ring exchange terms [51, 52] in promoting the spin liquid state is clearly warranted.

I. ACKNOWLEDGMENT

We thank MHRD and Department of Science and Technology, Govt. of India for financial support. We also thank Nandini Trivedi and Subhro Bhattacharjee for useful discussion and late Christoph Klausnitzer for technical support. Experiments at the ISIS Neutron and Muon Source were supported by a beam-time allocation RB1910129 from the Science and Technology Facilities Council. SP acknowledges financial support from Industrial Research and Consultancy Centre, IIT Bombay (17IRCCSG011) and SERB, DST, India (SRG/2019/001419). IDG acknowledges financial support from Technical Research Centre, DST and SERB India. AVM, IDG and SP acknowledge hospitality and support of ICTS and APCTP during the 2nd Asia Pacific Workshop on Quantum Magnetism (Code:ICTS/apfm2018/11).

* Electronic address: skundu37@gmail.com
† Electronic address: mahajan@phy.iitb.ac.in

[1] P. Fazekas and P. W. Anderson, Philos. Mag. **30**, 423 (1974).
[2] Y. Zhou, K. Kanoda, and T.-K. Ng, Rev. Mod. Phys. **89**, 025003 (2017).
[3] H. Kadowaki, H. Takei, and K. Motoya, J. Phys. Condens. Matter **7**, 6869 (1995).
[4] R. Ishii, S. Tanaka, K. Onuma, Y. Nambu, M. Tokunaga, T. Sakakibara, N. Kawashima, Y. Maeno, C. Broholm, D. P. Gautreaux, J. Y. Chan, and S. Nakatsuji, Europhys. Lett. **94**, 17001 (2011).
[5] Y. Shirata, H. Tanaka, A. Matsuo, and K. Kindo, Phys. Rev. Lett. **108**, 057205 (2012).
[6] D. A. Huse and V. Elser, Phys. Rev. Lett. **60**, 2531 (1988).
[7] T. Jolicoeur and J. C. Le Guillou, Phys. Rev. B **40**, 2727 (1989).
[8] R. R. P. Singh and D. A. Huse, Phys. Rev. Lett. **68**, 1766 (1992).
[9] B. Bernu, P. Lecheminant, C. Lhuillier, and L. Pierre, Phys. Rev. B **50**, 10048 (1994).
[10] L. Capriotti, A. E. Trumper, and S. Sorella, Phys. Rev. Lett. **82**, 3899 (1999).
[11] R. Kaneko, S. Morita, and M. Imada, J. Phys. Soc. Jpn. **83**, 093707 (2014).
[12] Z. Zhu and S. R. White, Phys. Rev. B **92**, 041105(R) (2015).
[13] Y. Iqbal, W.-J. Hu, R. Thomale, D. Poilblanc, and F. Becca, Phys. Rev. B **93**, 144411 (2016).
[14] J. Knolle and R. Moessner, Annu. Rev. Condens. Matter Phys. **10**, 451 (2019).
[15] Y. Shimizu, K. Miyagawa, K. Kanoda, M. Maesato, and G. Saito, Phys. Rev. Lett. **91**, 107001 (2003).
[16] T. Itou, A. Oyamada, S. Maegawa, Z. Tamura, and R. Kato, J. Phys. Condens. Matter **19**, 145247 (2007).
[17] T. Itou, A. Oyamada, S. Maegawa, M. Tamura, and R. Kato, Phys. Rev. B **77**, 104413 (2008).
[18] S. Yamashita, Y. Nakazawa, M. Oguni, Y. Oshima, H. Nojiri, Y. Shimizu, K. Miyagawa, and K. Kanoda, Nature Physics **4**, 459 (2008).
[19] J. A. Paddison, M. Daum, Z. Dun, G. Ehlers, Y. Liu, M. Stone, H. Zhou, and M. Mourigal, Nature Physics **13**, 117 (2017).
[20] M. Baenitz, P. Schlender, J. Sichelschmidt, Y. A. Onykiienko, Z. Zangeneh, K. M. Ranjith, R. Sarkar, L. Hozoi, H. C. Walker, J.-C. Orain, H. Yasuoka, J. van den Brink, H. H. Klauss, D. S. Inosov, and T. Doert, Phys. Rev. B **98**, 220409(R) (2018).
[21] R. Sarkar, P. Schlender, V. Grinenko, E. Haeussler, P. J. Baker, T. Doert, and H.-H. Klauss, Phys. Rev. B **100**, 241116(R) (2019).
[22] H. D. Zhou, E. S. Choi, G. Li, L. Balicas, C. R. Wiebe, Y. Qiu, J. R. D. Copley, and J. S. Gardner, Phys. Rev. Lett. **106**, 147204 (2011).
[23] Y. Ishiguro, K. Kimura, S. Nakatsuji, S. Tsutsui, A. Q. R. Baron, T. Kimura, and Y. Wakabayashi, Nature Communications **4**, 2022 (2013).
[24] A. A. Bush and V. P. Sirotinkin, Inorganic Materials **44**, 1233 (2008).
[25] D. C. Wallace and T. M. McQueen, Dalton Trans. **44**, 20344 (2015).
[26] J. T. Rijssenbeek, S. Malo, V. Caignaert, and K. R. Poeppelmeier, J. Am. Chem. Soc. **124**, 2090 (2002).
[27] J. R. Carvajal, Abstracts of the Satellite Meeting on Powder Diffraction of the XV Congress of the IUCr (1990), unpublished.
[28] For details see Supplemental Material, which includes Refs. [53–56].
[29] N. Elstner, R. R. P. Singh, and A. P. Young, Phys. Rev. Lett. **71**, 1629 (1993).
[30] M. Tamura and R. Kato, J. Phys. Condens. Matter **14**, L729 (2002).
[31] Y. Haraguchi, C. Michioka, M. Imai, H. Ueda, and K. Yoshimura, Phys. Rev. B **92**, 014409 (2015).
[32] Sub-dominant exchange couplings are assumed to not affect the susceptibility significantly in the *high-temperature* regime which is primarily controlled by the dominant exchange coupling.
[33] A CW fit at high-T, yields χ_0 = -1.61× 10^{-4} cm^3/mol Cu, C = 0.384 K cm^3/mol Cu and the θ_{CW} = -143 K. The inferred effective moment μ_{eff} = 1.75 μ_B is close to the expected value of 1.73 μ_B for S = 1/2 Cu^{2+} ion with g = 2. A negative θ_{CW} indicates antiferromagnetic correlations between the Cu^{2+} ions.
[34] Similar conclusions were drawn from our electron spin resonance (ESR) and nuclear magnetic resonance (NMR) experiments (see SM [28]).

[35] Y. Li, D. Adroja, P. K. Biswas, P. J. Baker, Q. Zhang, J. Liu, A. A. Tsirlin, P. Gegenwart, and Q. Zhang, Phys. Rev. Lett. **117**, 097201 (2016).

[36] M. A. de Vries, K. V. Kamenev, W. A. Kockelmann, J. Sanchez-Benitez, and A. Harrison, Phys. Rev. Lett. **100**, 157205 (2008).

[37] T.-H. Han, R. Chisnell, C. J. Bonnoit, D. E. Freedman, V. S. Zapf, N. Harrison, D. G. Nocera, Y. Takano, and Y. S. Lee, (2014), http://arxiv.org/abs/1402.2693v1 .

[38] A quadratic temperature dependence of the magnetic specific heat was seen in high-pressure prepared cubic phase of $S = 1$ $Ba_3NiSb_2O_9$ [57]. This observation was completely field-independent *unlike* our $S = \frac{1}{2}$ observations. Such field-independent quadratic dependence is thought to arise from quadrupolar ordering in pristine $S = 1$ triangular systems, however the triangular planes are diluted in the compound $Ba_3NiSb_2O_9$.

[39] Y.-M. Lu, Phys. Rev. B **93**, 165113 (2016).

[40] This estimate for the scale of J_1 is in the high temperature side of the specific heat data, thus the approximations of using the low energy form of the spectrum and $T \to 0$ are justified *a posteriori*.

[41] Y. Ran, M. Hermele, P. A. Lee, and X.-G. Wen, Phys. Rev. Lett. **98**, 117205 (2007).

[42] D. H. Kim, P. A. Lee, and X.-G. Wen, Phys. Rev. Lett. **79**, 2109 (1997).

[43] J. P. Perdew, K. Burke, and M. Ernzerhof, Phys. Rev. Lett. **77**, 3865 (1996).

[44] V. I. Anisimov, J. Zaanen, and O. K. Andersen, Phys. Rev. B **44**, 943 (1991).

[45] G. Kresse and J. Hafner, Phys. Rev. B **47**, 558 (1993).

[46] G. Kresse and J. Furthmüller, Phys. Rev. B **54**, 11169 (1996).

[47] P. E. Blöchl, Phys. Rev. B **50**, 17953 (1994).

[48] G. Kresse and D. Joubert, Phys. Rev. B **59**, 1758 (1999).

[49] H. J. Xiang, E. J. Kan, S.-H. Wei, M.-H. Whangbo, and X. G. Gong, Phys. Rev. B **84**, 224429 (2011).

[50] R. Kumar, T. Dey, P. M. Ette, K. Ramesha, A. Chakraborty, I. Dasgupta, R. Eremina, S. Tóth, A. Shahee, S. Kundu, M. Prinz-Zwick, A. A. Gippius, H. A. K. von Nidda, N. Büttgen, P. Gegenwart, and A. V. Mahajan, Phys. Rev. B **99**, 144429 (2019).

[51] O. I. Motrunich, Phys. Rev. B **72**, 045105 (2005).

[52] T. Grover, N. Trivedi, T. Senthil, and P. A. Lee, Phys. Rev. B **81**, 245121 (2010).

[53] K. Momma and F. Izumi, J. Appl. Cryst. **44**, 1272 (2011).

[54] Y. Han, M. Hagiwara, T. Nakano, Y. Nozue, K. Kimura, M. Halim, and S. Nakatsuji, Phys. Rev. B **92**, 180410(R) (2015).

[55] K. Y. Zeng, L. Ma, Y. X. Gao, Z. M. Tian, L. S. Ling, and L. Pi, Phys. Rev. B **102**, 045149 (2020).

[56] X.-G. Wen, *Quantum Field Theory of Many-Body Systems: From the Origin of Sound to an Origin of Light and Electrons* (Oxford University Press, 2007).

[57] J. G. Cheng, G. Li, L. Balicas, J. S. Zhou, J. B. Goodenough, C. Xu, and H. D. Zhou, Phys. Rev. Lett. **107**, 197204 (2011).

Supplementary Material for Gapless quantum spin liquid in the triangular system $Sr_3CuSb_2O_9$

S. Kundu,[1,*] Aga Shahee,[1] Atasi Chakraborty,[2] K. M. Ranjith,[3] B. Koo,[3] Jœrg Sichelschmidt,[3] Mark T.F. Telling,[4] P. K. Biswas,[4] M. Baenitz,[3] I. Dasgupta,[2] Sumiran Pujari,[1] and A. V. Mahajan[1,†]

[1]*Department of Physics, Indian Institute of Technology Bombay, Powai, Mumbai 400076, India*
[2]*School of Physical Sciences, Indian Association for the Cultivation of Science, Jadavpur, Kolkata 700032, India*
[3]*Max Planck Institute for Chemical Physics of Solids, 01187 Dresden, Germany*
[4]*ISIS Pulsed Neutron and Muon Source, STFC Rutherford Appleton Laboratory, Harwell Campus, Didcot, Oxfordshire OX110QX, UK*

(Dated: January 24, 2022)

Polycrystalline $Sr_3CuSb_2O_9$ (SCSO) sample was prepared by conventional solid state reaction techniques with high purity ingredients. X-ray diffraction showed the presence of superlattice reflections. We have then followed up with magnetisation, heat capacity, muon spin relaxation (μSR), electron spin resonance (ESR), and ^{121}Sb nuclear magnetic resonance (NMR) measurements. These are backed up by density functional theory (DFT) calculations and predictions based on a Dirac spin liquid ansatz to build a comprehensive picture of the properties of SCSO. We delve into various details in the following sections.

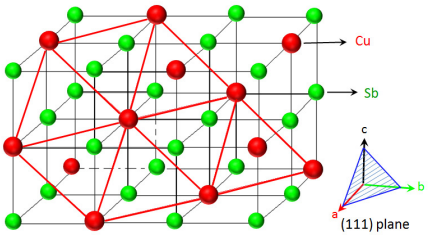

Figure 1: The edge-shared triangular lattice network of Cu^{2+} atoms in the (111) plane of the simple cubic lattice considering 1:2 cation ordering at the B-site in the triple perovskite $Sr_3CuSb_2O_9$.

I. X-RAY DIFFRACTION AND CRYSTAL STRUCTURE

The cubic perovskites are expressed by the general chemical formula ABX_3. One will notice that the (111) planes present an edge-shared triangular geometry. In real materials, in order to accommodate ions of various radii, rotation and tilting of the BO_6 octahedra takes place resulting in a lower than cubic symmetry for the crystal structure. In the present case, the B site is occupied by Cu and Sb ions. With 1:2 cation ordering at the B-site, the (111) planes in the pseudocubic lattice will have successive Cu planes separated by two Sb planes. These planes have an edge-shared triangular geometry (shown in Fig. 1) which is geometrically frustrated.

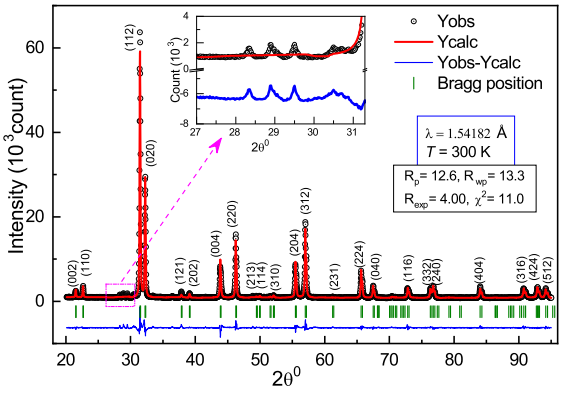

Figure 2: Rietveld refinement of powder XRD pattern of $Sr_3CuSb_2O_9$ is shown along with Bragg positions with corresponding Miller indices (hkl). Inset shows the unindexed peaks at low angles which might be originating from the superlattice reflections.

The Rietveld refinement of $Sr_3CuSb_2O_9$ by Fullprof suite software [1], in the body-centered tetragonal structure with space group $I4/mcm$ (140), is shown in Fig. 2. Atomic co-ordinates with site and occupancy of each element of $Sr_3CuSb_2O_9$ are given in Table II. The goodness of the Rietveld refinement is defined by the following parameters: $\chi^2 = 11.0$; R_p= 12.6%; R_{wp}= 13.3%; R_{exp}= 4.00%. A few unindexed (possibly superlattice) peaks at low angles ($2\theta < 30^o$) are shown in the inset of Fig. 2. To determine the possible propagation vector corresponding to these superlattice peaks, we performed a propagation vector ($\vec{K}$) search and fitting. During this $\vec{K}$-search and $\vec{K}$-vector fitting, the lattice parameters were fixed to the refined values of the tetragonal lattice with space group $I4/mcm$. However, a lower symmetry spacegroup $P\bar{1}$ (triclinic) was used to allow all possible superlattice reflections. The LeBail fit was employed for the $\vec{K}$-search. We could then index the additional reflections as superlattice reflections with $\vec{K}$ = (1/3, 1/3, 1/3) and index the full pattern. Note that the structure of SCSO is quite different from the various (either with the triangu-

Table I: Obtained parameters after Rietveld refinement.

Space group	$I4/mcm$	$P\bar{1}$
Propagation vector	None	$\vec{K} = (\frac{1}{3}, \frac{1}{3}, \frac{1}{3})$
Lattice parameter	$a = b = 5.547$ Å	$a = b = 5.547$ Å
	$c = 8.248$ Å	$c = 8.248$ Å
α, β, γ	$\alpha = \beta = \gamma = 90^o$	$\alpha = \beta = \gamma = 90^o$
Cell volume [Å^3]	253.7844	253.7844
R_p, R_{wp}, R_{exp}(%)	12.6, 13.3, 4.00	9.76, 10.7, 4.50
Bragg R-factor	3.06	0.75
RF-factor	3.00	1.05
χ^2	11.0	5.62

lar or honeycomb Cu-planes) structures of $Ba_3CuSb_2O_9$ (BCSO). In BCSO, the basal $a-b$ plane has a triangular magnetic lattice whereas for SCSO it is the (111) planes which present the triangular lattice. Another illustration of the crystal structure (using the Vesta software [2]) is shown in Fig. 3.

Table II: Atomic coordinates in $Sr_3CuSb_2O_9$ based on a $I4/mcm$ space group refinement.

Atom	Wyckoff position	x	y	z	Occupancy
Sr	4b	0.000	0.500	0.250	1.000
Cu	4c	0.000	0.000	0.000	0.333
Sb	4c	0.000	0.000	0.000	0.667
O1	8h	0.794	0.294	0.000	1.000
O2	4a	0.000	0.000	0.250	1.000

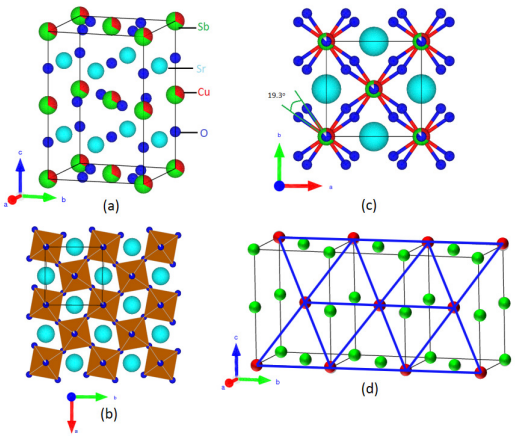

Figure 3: Structure of $Sr_3CuSb_2O_9$ (a) One tetragonal unit cell showing the mixed B-site which is occupied by both Sb^{5+} and Cu^{2+} ions, (b) Tilted corner-shared (Cu/Sb) O_6 octahedra in ab-plane. (c) Top view of one unit cell along c-axis, showing the tilting angle of 19.3° between consecutive CuO_6 octahedra. (d) Edge-shared triangular lattice network of Cu^{2+} ions considering 1:2 cation ordering at the B-site of the perovskite.

II. MAGNETIZATION

We measured the dc magnetization $M(T)$ as a function of temperature in the range 2-300 K on a hard pellet of SCSO in zero field cooled (ZFC) and field cooled (FC) mode at several magnetic fields (H) using a Quantum Design MPMS system. The main features of our observations from the measurements are described below. The

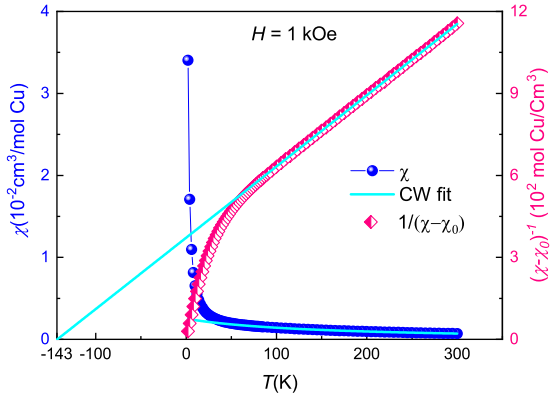

Figure 4: The left y-axis shows the temperature dependence of $\chi(T) = \frac{M(T)}{H}$ (blue circles) of SCSO measured in $H = 1$ kOe and the right y-axis shows the inverse susceptibility free from the temperature independent susceptibility χ_0. The Curie-Weiss (CW) fit is shown in the temperature range 150 - 300 K with a cyan solid line. The intercept on the x-axis gives a CW temperature $\theta_{CW} \simeq$ -143 K.

susceptibility of SCSO (Fig. 4) was analysed initially using $\chi = \chi_0 + \frac{C}{T-\theta_{CW}}$; where χ_0, C and θ_{CW} are temperature independent susceptibility (arising from the diamagnetic core (χ_{core}) and paramagnetic van-Vleck (χ_{VV}) contributions), Curie constant, and the Curie-Weiss temperature, respectively. A fit in the range of 150 - 300 K gave χ_0= -1.61× 10^{-4} (cm^3/mol Cu), C = 0.384 (Kcm^3/mol Cu) and the $\theta_{CW} = -143$ K. From the Curie constant, we obtained the effective moment $\mu_{eff} = 1.75\,\mu_B$ which is close to the expected value of $\mu_{eff} = 1.73\,\mu_B$ for $S = \frac{1}{2}$ Cu^{2+} ion. The negative value of CW temperature indicates antiferromagnetic correlations between the Cu^{2+}

magnetic ions. Given that there is no order down to 65 mK (see μSR analysis in a latter section), this gives a very high frustration parameter ($f = \frac{\theta_{CW}}{T_N}$ >2000). The

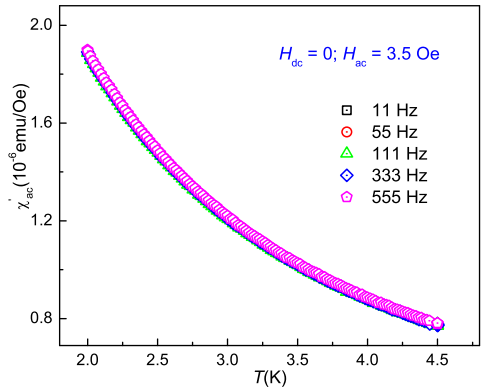

Figure 5: The in phase component of the ac susceptibility of SCSO as a function of temperature at various frequencies.

ac susceptibility of SCSO was measured to ensure that there is no glassy behaviour at low temperature. Fig. 5 shows the in-phase component of a.c. susceptibility as a function of temperature at different frequencies with an a.c. field of 3.5 Oe amplitude and zero d.c. applied field. No anomaly is seen excluding the presence of a glassy phase down to 1.8 K.

III. ELECTRON SPIN RESONANCE

Electron spin resonance (ESR) is another microscopic probe for magnetism. ESR can probe the spin dynamics of the very spin system in contrast to NQR and μSR, both of which access the spin system indirectly. Thus, ESR has proven to provide direct access to the spin dynamics of many systems. Here, the ESR experiments probe the Cu^{2+} spins of SCSO at X-band frequencies ($\nu = 9.4$ GHz) using a continuous-wave ESR spectrometer. The sample was measured as a powder embedded in paraffine and the temperature was set with a helium-flow cryostat allowing for temperatures between 3 K and 290 K.

Typical ESR spectra (given as the first derivative of the absorbed microwave power) of SCSO are shown in the left panel of Fig. 6 for selected temperatures. The lines could reasonably be fitted by a Lorentzian shape, averaged for uniaxial g-factor anisotropy, as shown by the solid lines. This yield the linewidth ΔB which is a measure of the spin-probe relaxation rate, and the resonance field B_{res} which is determined by the effective g-factor ($g_{ESR} = h\nu/\mu_B B_{res}$) and internal fields. Below $T \simeq 80$ K the spectra reveal additional lines which indicate the presence of Cu^{2+} spins in a lower than uniaxial environmental symmetry. These results are similar to those in $Ba_3CuSb_2O_9$ [3]. At higher temperatures and below about 5 K these structures becomes smeared out by line broadening. As shown in the right panel of Fig. 6 both the linewidth ΔB and g_{ESR} show a considerable temperature dependence below $T \simeq 10$ K, indicating emergent spin fluctuations and internal magnetic fields. For $T = 290$ K we obtained $g_{\parallel} = 2.08$ and $g_{\perp} = 2.31$, corresponding to an averaged value $g_{avg} = \sqrt{(g_{\parallel}^2 + 2g_{\perp}^2)/3} = 2.24$ which is typical of Cu^{2+} for many cuprate systems. The ESR intensity I_{ESR} corresponds to the integrated ESR absorption and is determined by the static spin-probe susceptibility, *i.e.* it provides a direct microscopic probe of the sample magnetization. The right panel of Fig. 6 also shows the temperature dependence of I_{ESR}^{-1} which follows the measured susceptibility very well with a Weiss temperature of −143 K for the high temperature behavior.

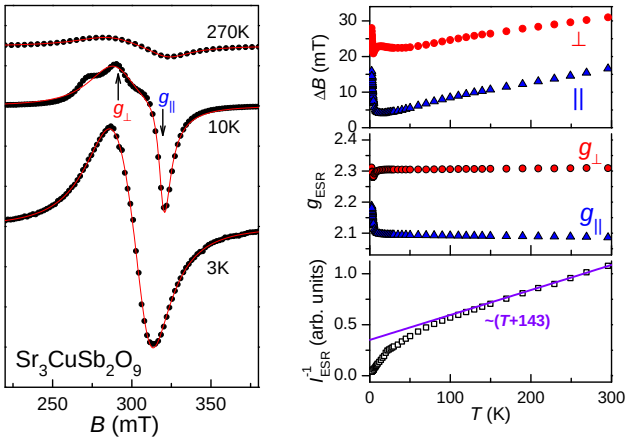

Figure 6: Left panel: X-band ESR spectra (symbols) at representative temperatures and fitted uniaxial powder-averaged Lorentzians (solid lines). Fitted values of anisotropic g-values are indicated for the spectrum at $T = 10$ K. Right panel: Temperature dependence of fitted parameters linewidth, effective g-value, and inverse integrated ESR intensity with Curie-Weiss behavior as indicated by the solid line.

IV. HEAT CAPACITY

Fig. 7 shows the $C_p(T)$ vs. T plot in different fields. For clarity, we have shown $C_p(T)$ vs. T plot in log-log scale in the inset (a) of Fig. 7. Also, we have plotted $C_p(T)/T$ vs. T in the inset (b) of Fig. 7, which indicates the presence of the Schottky anomaly below 9 K due to free spins within the system as the peak position is shifted gradually towards high temperature as field strength increases. Since we do not have a suitable non-magnetic analog of this system, to obtain the lattice contribution, we fitted the heat capacity in zero field in the high-T region (such as 50 -130 K) to a combination of one Debye and three Einstein (1D+3E) functions (see later). This was then extrapolated to lower temperatures for analysing the low-T data. A βT^3 variation of

the lattice heat capacity was seen (for $T < 6$ K) from this extrapolation. The value of β depends somewhat on the high-T fitting range used for the lattice fit but is around 3×10^{-4} J/mol K^4. Using this value good fits of the measured data to $C_{\rm p}(T) = \gamma T + \alpha T^2 + \beta T^3 + f C_{\rm Schottky}$ are obtained (see Fig.8). The variation of the inferred Schottky gap with the applied field is shown in Fig. 9.

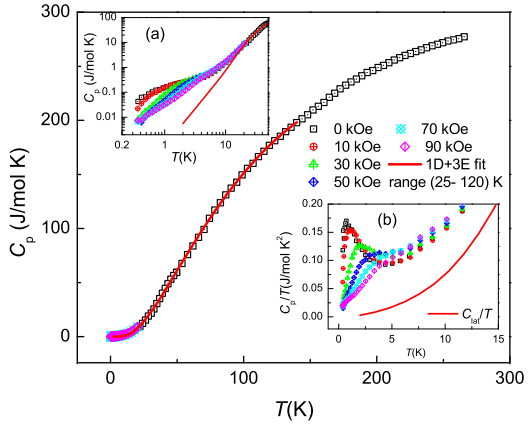

Figure 7: Heat capacity of SCSO at different fields with Debye plus Einstein fitting. Inset (a) shows the same data on a log-log scale. In inset (b), $C_{\rm p}/T$ vs. T shows low temperature anomaly due to Schottky effect.

We used a combination of Debye and Einstein terms as expressed by the Eq. 1 and 2 to estimate the lattice contribution $C_{\rm lat}$. Here, $C_{\rm D}$ and $C_{\rm E_i}$ are the weightage factors corresponding to acoustic and optical modes of atomic vibrations and $\theta_{\rm D}$, $\theta_{\rm E_i}$ are the corresponding Debye and Einstein temperatures, respectively.

$$C_{\rm Debye}(T) = C_{\rm D}\left[9R(\frac{T}{\theta_{\rm D}})^3 \int_0^{x_{\rm D}} \frac{x^4 e^x}{(e^x-1)^2} dx\right] \quad (1)$$

$$C_{\rm Einstein}(T) = \sum C_{\rm E_i}\left[3R(\frac{\theta_{\rm E_i}}{T})^2 \frac{exp(\frac{\theta_{\rm E_i}}{T})}{(exp(\frac{\theta_{\rm E_i}}{T})-1)^2}\right] \quad (2)$$

We obtained the weightage factors in the ratio: $C_{\rm D}$:$C_{\rm E_1}$:$C_{\rm E_2}$:$C_{\rm E_3}$ = 1:1:5:6. The total sum of $C_{\rm D}+\sum C_{\rm E_i}$ is equal to 13 which is close to the total number of atoms (15) per formula unit of SCSO. The fitting also yields the Debye temperature $\theta_{\rm D}$= (140±1) K and the Einstein temperatures; $\theta_{\rm E_1}$= (109±1) K, $\theta_{\rm E_2}$= (219±2) K and $\theta_{\rm E_3}$= (436±2) K.

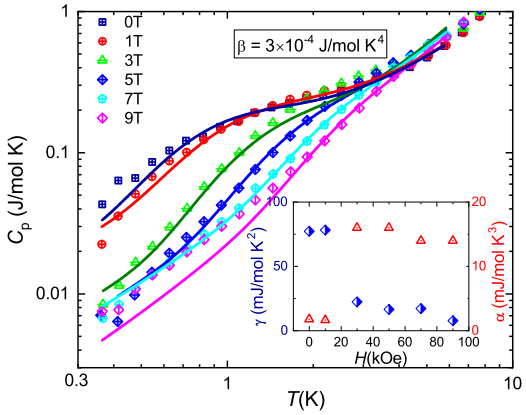

Figure 8: The specific heat of SCSO is shown together with fits (solid lines) as described in the text. The inset shows the variation of γ and α with H.

In Fig.8, we have fitted the C_p vs. T by Eq. 3.

$$C_p = \gamma T + \alpha T^2 + \beta T^3 + f C_{\rm Sch} \quad (3)$$

where $C_{\rm Sch}$ is for two level system with S =1/2.

$$C_{\rm Sch} = \left[R(\frac{\Delta}{k_{\rm B}T})^2 \frac{exp(\frac{\Delta}{k_{\rm B}T})}{[1+exp(\frac{\Delta}{k_{\rm B}T})]^2}\right] \quad (4)$$

Here f is the fraction of free spins within the system, Δ is the Schottky gap, R is the universal gas constant, $k_{\rm B}$ is the Boltzmann constant.

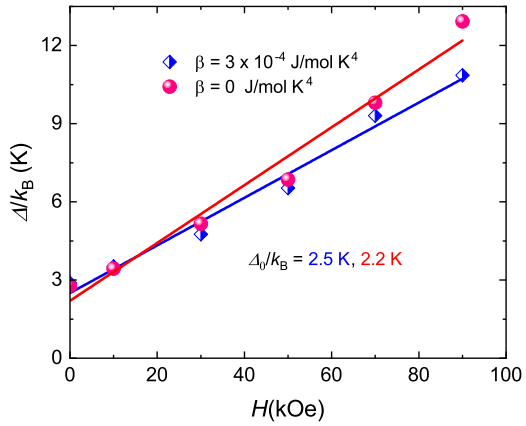

Figure 9: Linear variation and fit of Schottky gap for both values of β. They show intrinsic interaction present in the system as in 0 kOe field we get a non-zero intercept close to 2.5 K.

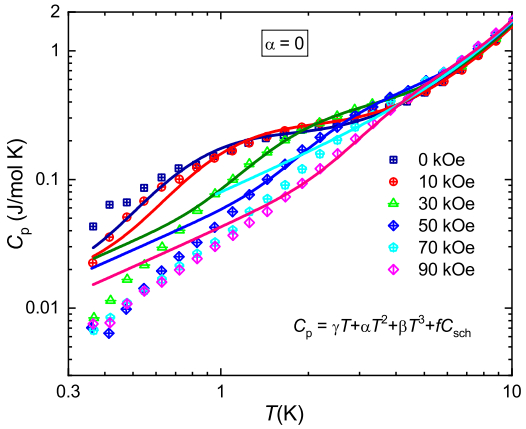

Figure 10: The specific heat data of SCSO for all fields are shown with fits for $\alpha = 0$ as mentioned in the text.

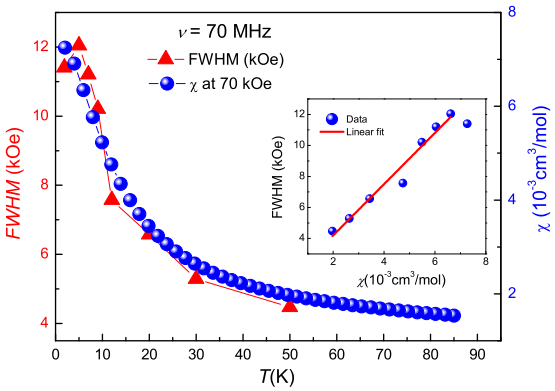

Figure 12: FWHM of ^{121}Sb NMR line (left y-axis) in SCSO is shown as a function of temperature together with the dc susceptibility at 70 kOe (right y-axis). The inset shows that the FWHM scales with the susceptibility with temperature as an implicit parameter.

V. NUCLEAR MAGNETIC RESONANCE

NMR is a useful probe of low energy excitations in magnetic insulators. For a recent example of a NMR study on a triangular system, see Ref. [4]. In our system, the ^{121}Sb nucleus has a nuclear spin of $I = \frac{5}{2}$, natural abundance is 57.25% and $\frac{\gamma}{2\pi} = 10.19$ MHz/Tesla. In our 94 kOe fixed field NMR set up, we have initially checked the spectra at different temperatures. As it was broader than 4 MHz at 80 K it was not possible to get the full NMR line shape by single Fourier transform of the spin echo. Also the ^{121}Sb NMR signal is very weak at high temperature, and above 50 K it really requires a large number of scans for a reasonable signal to noise ratio which is very much time-consuming. We then measured ^{121}Sb NMR spectra by sweeping magnetic field at temperatures below $T = 50$ K.

1. ^{121}Sb NMR Spectra

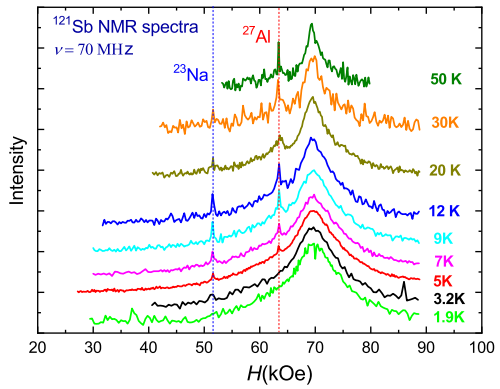

Figure 11: Field swept ^{121}Sb NMR spectra of $Sr_3CuSb_2O_9$ at various temperatures.

We have measured field swept NMR spectra of ^{121}Sb nucleus from 50 K to 2 K (shown in Fig. 11) at a fixed frequency $\nu = 70$ MHz. From the plot, it is clear that there is no significant NMR line shift of the peak position as temperature decreases. The spectrum broadens as temperature decreases. This broadening is likely due to ^{121}Sb nuclear-Cu^{2+} local moment dipolar interaction. In each spectrum, there are spikes at 63.4 kOe and 51.6 kOe. These do not shift with temperature and may be from the probe head or the sample holder. To be sure, we performed measurements under the same conditions after removing the sample from the sample holder. Then we noticed that these signals were present without sample also. It appears that the signals at 63.4 kOe and 51.6 kOe are from ^{27}Al and ^{23}Na nuclei which are present in the probe head. The FWHM of the ^{121}Sb NMR line shape is plotted with temperature and it follows the bulk dc susceptibility at 70 kOe (shown in Fig. 12). The inset of Fig. 12 shows the linearity of FWHM with bulk susceptibility data at 70 kOe.

2. Spin-lattice relaxation

Fig. 13(a) shows the saturation recovery of the longitudinal component of ^{121}Sb nuclear magnetization *i.e.* the spin-lattice relaxation (T_1) from 30 K to 2 K. Using a pulse comb to saturate the broad line, we could obtain about 80% saturation of the signal. The nuclear magnetization recovery is well fitted with a stretched exponential ($M(t) = M_0[1 - A\,exp(\frac{-t}{T_1})^{\beta}]$). The stretching exponent is around $\beta \approx 0.60$ (shown in the inset of Fig. 13(a)). There is no significant change in values of T_1 with temperatures and the average T_1 is around 650 μs. The spin-lattice re-

laxation rate is shown in Fig. 13(b). $1/T_1T$ follows a Curie-Weiss like the bulk susceptibility. For Dirac quasiparticles (linear dispersion) in two-dimensions, the NMR spin-lattice relaxation rate (which depends on the square of the density-of-states) should show a power-law with T ($1/T_1 \propto T^3$). However, our measurements are only down to about 2 K. Perhaps, lower temperatures are required to observe this contribution. Another point is that NMR measurements are in an applied magnetic field which is also expected to affect the quasiparticle spectrum.

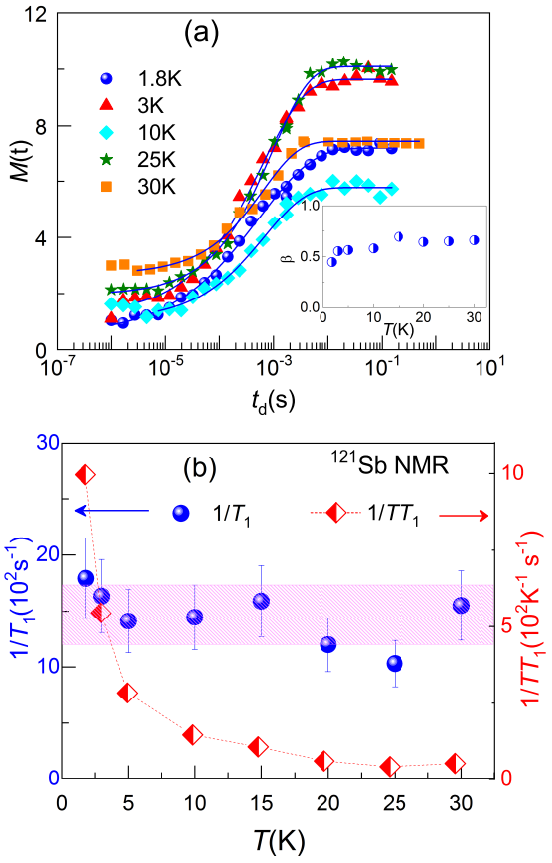

Figure 13: Recovery of the longitudinal nuclear magnetization for ^{121}Sb as a function of delay time after a saturating pulse sequence. The solid lines show fits to stretched exponentials. Inset shows the variation of the stretching exponent β. (b) The spin-lattice relaxation rate ($1/T_1$) is seen to be nearly independent of temperature. $1/T_1T$ varies in a Curie-Weiss-like manner. The dashed line is a guide to the eye.

VI. μSR RESULTS

The width of the Gaussian in the Kubo-Toyabe function from a fit of the ZF data at 4.5 K is about 0.12 MHz. This amounts to a field of about 1.4 Oe at the muon site which is a typical value for the field from nuclear moments (Cu in this case). Next, data were taken in various longitudinal fields to check how the muons decouple from the internal fields.

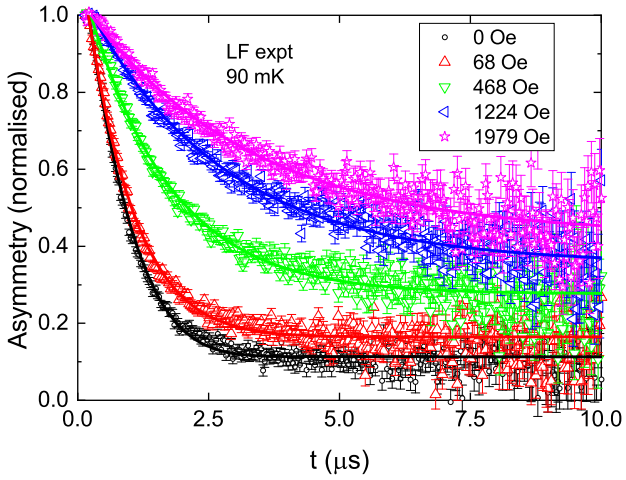

Figure 14: The variation of the muon asymmetry with time is shown in some selected longitudinal fields at about 90 mK for $Sr_3CuSb_2O_9$. The solid lines are fits as explained in the text.

From the data in Fig. 14, it can be seen that even in a large field of 1979 Oe, the muons are still not decoupled from the internal fields. This indicates that the moments remain dynamic down to the lowest temperatures studied. These are typical signatures seen in quantum spin liquid materials. The LF data were also fit to the product of the KT function with an exponential in addition to a constant background. The muon depolarisation rate thus obtained is plotted as a function of the magnetic field in Fig. 15.

At very high fields one expects muons to totally decouple from the internal fields resulting in no relaxation. But as seen in Fig. 15, a field of 1979 Oe is not at all sufficient to make λ near negligible. Following the analysis of the field dependence of λ as in Ref. [5], we fit the data to the following equation:

$$\lambda(H) = 2\Delta^2\tau^x \int_0^\infty t^{-x} exp(-\nu t)\cos(\gamma_\mu H t)dt \qquad (5)$$

where ν is the fluctuation frequency of local moments and Δ is the distribution width of the local magnetic fields. The muon gyromagnetic ratio is $\gamma_\mu = 2\pi$ x 135.5342 MHz/T. A fit with $x = 0$ (red dashed curve in Fig. 15) which implies an exponential auto-correlation function $S(t) \sim exp(-\nu t)$ does not fit the data well and rather $S(t) \sim (\tau/t)^x exp(-\nu t)$ is needed to fit the data. The black solid curve is a fit to Eq. 5 and gives $x = 0.56$ and $\nu = 1.8 \times 10^7 Hz$. τ is the early time cut-off and is fixed to 1 ps. This result implies the presence of long-time spin

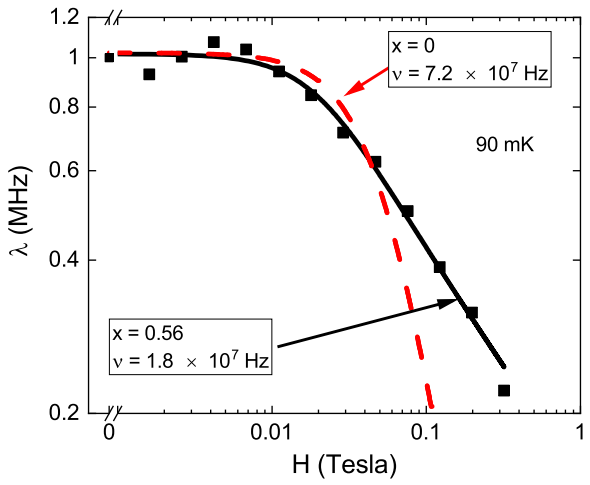

Figure 15: The variation of the muon relaxation rate at 90 mK is shown as a function of the longitudinal magnetic field for $Sr_3CuSb_2O_9$. The black curve is a fit to Equation 5 with x as a fitting parameter and the red dashed curve is a fit to the same equation but with x = 0.

correlations but without any static order; a hallmark of spin liquids. While the numerical values above are similar to those found in $YbMgGaO_4$ [5], we note that muon relaxation in SCSO is well fit to a single exponential (implying uniform relaxation for all muons) in contrast to $YbMgGaO_4$ where a stretched exponential behavior (implying a distribution of relaxation rates perhaps due to a distribution of environments) was found.

VII. DETAILS OF DIRAC QUANTUM SPIN LIQUID ANSATZ

For the Hamiltonian $\mathcal{H} = \sum_{\langle i,j\rangle\in\triangle} J\mathbf{S}_i\cdot\mathbf{S}_j + \ldots$ on the triangular lattice, where $\ldots$ stands for further neighbor interactions providing frustration, the following effective mean-field Hamiltonian is postulated as an anstaz

$$\begin{aligned}\mathcal{H} &= \frac{J_{\text{eff}}}{2}\sum_{\langle i,j\rangle\in\triangle \text{ lattice},\sigma}\chi_{ij}c^\dagger_{i,\sigma}c_{j,\sigma} + \text{ h.c.}\\ &= \frac{J_{\text{eff}}}{2}\sum_{\mathbf{k}\in \text{ B. Z.},\sigma} C^\dagger_{\mathbf{k},\sigma}\cdot H_{\mathbf{k}}\cdot C_{\mathbf{k},\sigma}\end{aligned} \tag{6}$$

where $C_{\mathbf{k},\sigma} = (c_{\mathbf{k},1,\sigma} \quad c_{\mathbf{k},2,\sigma})^T$, $c_{\mathbf{k},\mu,\sigma} = \frac{1}{N_{\text{UCs}}}\sum_{\mathbf{r}_\mu\in\square \text{ lattice}} c_{\mathbf{r}_\mu,\sigma}e^{-i\mathbf{k}\cdot\mathbf{r}_\mu}$. Here, the mean-field decoupling procedure for fermionic spin liquids (see Chapter 9 of Ref. [6]) has been applied, and these fermionic degrees of freedom are termed as spinons. J_{eff} is an effective coupling parameter at the mean-field level. It is expected to be of the order of J_1. The "$\square$" lattice in the Fourier sum corresponds to the doubled unit cell that arises in the DSL ansatz (See Fig. 3a of Ref. 7). This gives rise to the μ index, and the Fourier sum for $c_{\mathbf{k},\mu,\sigma}$ runs over only μ type of sites. σ is the $S = \frac{1}{2}$ index. For the Dirac QSL ansatz defined via χ_{ij}, we follow the gauge choice of Ref. 7. The gauge-invariant fluxes still respect the symmetry of the $\triangle$ lattice, such that π-flux is present in the "up" triangles, and 0-flux is present in the "down" triangles. The resulting lattice thus is still chosen to have the same primitive lattice vectors as the underlying $\triangle$ lattice. Going to Fourier space we arrive at the matrix elements $h_{\mu\nu}(\mathbf{k})$ of the $H_{\mathbf{k}}$ matrix:

$$\begin{aligned}h_{11}(\mathbf{k}) &= 2\cos(\mathbf{k}\cdot\mathbf{a}_1)\\ h_{22}(\mathbf{k}) &= -2\cos(\mathbf{k}\cdot\mathbf{a}_1)\\ h_{12}(\mathbf{k}) &= 2\cos(\mathbf{k}\cdot\mathbf{a}_2) - 2i\sin(\mathbf{k}\cdot(\mathbf{a}_1+\mathbf{a}_2))\\ h_{21}(\mathbf{k}) &= h_{12}(\mathbf{k})^*\end{aligned} \tag{7}$$

or compactly, $H_{\mathbf{k}} = 2\cos(\mathbf{k}\cdot\mathbf{a}_1)\tau_z + 2\cos(\mathbf{k}\cdot\mathbf{a}_2)\tau_x + 2\sin(\mathbf{k}\cdot(\mathbf{a}_1+\mathbf{a}_2))\tau_y$ where the τ Pauli matrices operate on the μ indices, $\mathbf{a}_1 = (1,0)$, $\mathbf{a}_2 = (-\frac{1}{2},\frac{\sqrt{3}}{2})$ in units of the lattice constant (which we take to be dimensionless unity). Diagonlizing $H_{\mathbf{k}}$, we arrive at a single Dirac cone in the Brillouin Zone with a choice of primitive reciprocal lattice vectors as $\mathbf{b}_1 = 2\pi(1,\frac{1}{\sqrt{3}})$, $\mathbf{b}_2 = 2\pi(0,\frac{2}{\sqrt{3}})$ in units of inverse lattice constant. The eigenvalues of $H_{\mathbf{k}}$ are $\pm\sqrt{2}\left(\frac{J_{\text{eff}}}{2}\right)\left[3+\cos(2k_x)+2\sin(k_x)\sin(\sqrt{3}k_y)\right]^{1/2}$. Expanding near the Dirac cone at $\mathbf{k} = (\frac{\pi}{2},\frac{\sqrt{3}\pi}{2})$, we arrive the effective low energy spectrum $\pm\epsilon_{\mathbf{k}} \equiv \pm\epsilon_k = \pm\sqrt{6}\left(\frac{J_{\text{eff}}}{2}\right)k$. Note k is dimensionless since we take the lattice constant to be dimensionless unity. We have to stay at half-filling (on average at mean-field level). This is ensured by the zero chemical potential for this particle-hole symmetry spectrum.

With the low energy spectrum in hand, we can work out the specific heat contribution from the Dirac QSL:

$$
\begin{aligned}
E(T)-E(T=0) &= 2\left[\int_0^{\Lambda_k}\frac{d^2\mathbf{k}}{\mathcal{A}_{\rm UC}\mathcal{A}_{\rm BZ}}f(\epsilon_{\mathbf{k}})(+\epsilon_{\mathbf{k}})+\int_0^{\Lambda_k}\frac{d^2\mathbf{k}}{\mathcal{A}_{\rm UC}\mathcal{A}_{\rm BZ}}(f(-\epsilon_{\mathbf{k}})-1)(-\epsilon_{\mathbf{k}})\right]\\
&= \frac{2}{\pi}\int_0^{\Lambda_k}kdk\;\frac{\epsilon_k}{e^{\beta\epsilon_k}+1} = \frac{1}{3\pi\left(\frac{J_{\rm eff}}{2}\right)^2}\int_0^{\sqrt{6}\left(\frac{J_{\rm eff}}{2}\right)\Lambda_k}d\epsilon\;\frac{\epsilon^2}{e^{\beta\epsilon}+1}\\
&= \frac{1}{3\pi\left(\frac{J_{\rm eff}}{2}\right)^2\beta^3}\int_0^{\sqrt{6}\left(\frac{J_{\rm eff}}{2}\right)\Lambda_k\beta}dy\;\frac{y^2}{e^y+1} = \frac{1}{3\pi\left(\frac{J_{\rm eff}}{2}\right)^2\beta^3}\int_0^{\infty}dy\;\frac{y^2}{e^y+1}\;\;\text{as }\beta\to\infty\\
&\approx 0.191\frac{(k_BT)^3}{\left(\frac{J_{\rm eff}}{2}\right)^2} \qquad (8)\\
\implies \frac{C(T)}{k_B} &\approx 2.292\frac{(k_BT)^2}{J_{\rm eff}^2} \qquad (9)
\end{aligned}
$$

The factor of 2 outside the big square brackets in the first line above is due to summing over the spin quantum number $\sum_\sigma$. We may include an external applied field to the above analysis via a Zeeman coupling to the spins, i.e. $\mathcal{H}=J\sum_{\langle i,j\rangle\in\triangle}\mathbf{S}_i\cdot\mathbf{S}_j+g\mu_B\sum_i\mathbf{H}\cdot\mathbf{S}_i$. Again making the Dirac QSL ansatz and taking the spin quantization axis along the external magnetic field $\mathbf{H}$, we arrive at

$$
\begin{aligned}
\mathcal{H} &= \frac{J_{\rm eff}}{2}\sum_{\langle i,j\rangle\in\triangle\text{ lattice},\sigma}\chi_{ij}c^\dagger_{i,\sigma}c_{j,\sigma}+\text{ h.c.}+H'\sum_i\left(c^\dagger_{i,\uparrow}c_{j,\uparrow}-c^\dagger_{i,\downarrow}c_{j,\downarrow}\right)\\
&= \frac{J_{\rm eff}}{2}\sum_{\mathbf{k}\in\text{ B. Z.},\sigma}C^\dagger_{\mathbf{k},\sigma}\cdot H_{\mathbf{k},\sigma}\cdot C_{\mathbf{k},\sigma} \qquad (10)
\end{aligned}
$$

where H' is a lumped parameter with same dimensions as $J_{\rm eff}$ ($H'=g\mu_B|\mathbf{H}|/2$). Going to Fourier space as before, we arrive at the matrix elements $h_{\mu\nu,\sigma}(\mathbf{k})$ of the $H_{\mathbf{k},\sigma}$ matrix:

$$
\begin{aligned}
h_{11,\sigma}(\mathbf{k}) &= 2\cos(\mathbf{k}\cdot\mathbf{a}_1)+(-1)^\sigma\frac{H'}{\left(\frac{J_{\rm eff}}{2}\right)}\\
h_{22,\sigma}(\mathbf{k}) &= -2\cos(\mathbf{k}\cdot\mathbf{a}_1)+(-1)^\sigma\frac{H'}{\left(\frac{J_{\rm eff}}{2}\right)}\\
h_{12,\sigma}(\mathbf{k}) &= 2\cos(\mathbf{k}\cdot\mathbf{a}_2)-2i\sin(\mathbf{k}\cdot(\mathbf{a}_1+\mathbf{a}_2))\\
h_{21,\sigma}(\mathbf{k}) &= h_{12}(\mathbf{k})^* \qquad (11)
\end{aligned}
$$

or compactly, $H_{\mathbf{k},\sigma}=2\cos(\mathbf{k}\cdot\mathbf{a}_1)\tau_z+2\cos(\mathbf{k}\cdot\mathbf{a}_2)\tau_x+2\sin(\mathbf{k}\cdot(\mathbf{a}_1+\mathbf{a}_2))\tau_y+(-1)^\sigma\frac{H'}{\left(\frac{J_{\rm eff}}{2}\right)}\tau_0$. It is understood that $(-1)^\uparrow=1$, $(-1)^\downarrow=-1$ and τ_0 is the identity matrix in the μ index. Going through the same steps as before, we will now arrive at the effective low energy spectrum $\pm\epsilon_{\mathbf{k},\sigma}\equiv\pm\epsilon_{k,\sigma}=\pm\epsilon_k+(-1)^\sigma H'$, i.e. the applied field acts like a chemical potential with opposite sign for $\sigma=\uparrow$ and $\sigma=\downarrow$. With the low energy spectrum in hand, we can work out the specific heat contributions due to imbalanced occupations of the two spin species.[8]

The energy contributions are shown below:

$$
\begin{aligned}
E_\uparrow(T)-E_\uparrow(T=0) &= \left[\int_0^{\Lambda_k}\frac{d^2\mathbf{k}}{\mathcal{A}_{\rm UC}\mathcal{A}_{\rm BZ}}f(\epsilon_{\mathbf{k},\uparrow})(+\epsilon_{\mathbf{k},\uparrow})+\int_0^{k|_{\epsilon_k=H'}}\frac{d^2\mathbf{k}}{\mathcal{A}_{\rm UC}\mathcal{A}_{\rm BZ}}f(-\epsilon_{\mathbf{k},\uparrow})(-\epsilon_{\mathbf{k},\uparrow})\right.\\
&\quad\left.+\int_{k|_{\epsilon_k=H'}}^{\Lambda_k}\frac{d^2\mathbf{k}}{\mathcal{A}_{\rm UC}\mathcal{A}_{\rm BZ}}(f(-\epsilon_{\mathbf{k},\uparrow})-1)(-\epsilon_{\mathbf{k},\uparrow})\right] \qquad (12)\\
E_\downarrow(T)-E_\downarrow(T=0) &= \left[\int_{k|_{\epsilon_k=H'}}^{\Lambda_k}\frac{d^2\mathbf{k}}{\mathcal{A}_{\rm UC}\mathcal{A}_{\rm BZ}}f(\epsilon_{\mathbf{k},\downarrow})(+\epsilon_{\mathbf{k},\downarrow})+\int_0^{k|_{\epsilon_k=H'}}\frac{d^2\mathbf{k}}{\mathcal{A}_{\rm UC}\mathcal{A}_{\rm BZ}}(f(\epsilon_{\mathbf{k},\downarrow})-1)(\epsilon_{\mathbf{k},\downarrow})\right.\\
&\quad\left.+\int_0^{\Lambda_k}\frac{d^2\mathbf{k}}{\mathcal{A}_{\rm UC}\mathcal{A}_{\rm BZ}}(f(-\epsilon_{\mathbf{k},\downarrow})-1)(-\epsilon_{\mathbf{k},\downarrow})\right]
\end{aligned}
$$

For the above, we again follow similar steps as in Eq. 8 to arrive at the sum of the two contributions:

$$E(T,H) - E(T=0,H) \approx 0.191 \frac{(k_B T)^3}{\left(\frac{J_{\rm eff}}{2}\right)^2} + \frac{(k_B T)^3}{3\pi \left(\frac{J_{\rm eff}}{2}\right)^2} \int_0^{\beta H'} dy \frac{(\beta H' - y) y}{e^y + 1} \tag{13}$$

In the above, we have assumed $\beta J_{\rm eff} \to \infty$ similar to the zero field calculation in Eq. 8, while no such assumption is put on $\beta H'$. When $\beta H' \to 0$, we recover the T^2 behaviour in the specific heat as expected. When $\beta H' \to \infty$, we will get in the limiting case

$$\begin{aligned} E(T,H) - E(T=0,H) &\approx 0.191 \frac{(k_B T)^3}{\left(\frac{J_{\rm eff}}{2}\right)^2} + \frac{(k_B T)^2 H'}{3\pi \left(\frac{J_{\rm eff}}{2}\right)^2} \int_0^{\infty} dy \frac{y}{e^y + 1} \\ &\approx 0.191 \frac{(k_B T)^3}{\left(\frac{J_{\rm eff}}{2}\right)^2} + 0.087 \frac{(k_B T)^2 H'}{\left(\frac{J_{\rm eff}}{2}\right)^2} \\ \implies \frac{C(T,H)}{k_B} &\approx 2.292 \frac{(k_B T)^2}{J_{\rm eff}^2} + 0.696 \frac{(k_B T) H'}{J_{\rm eff}^2} \end{aligned} \tag{14}$$

We have neglected the $-\frac{y\left(\frac{y}{\beta H'}\right)}{e^y+1}$ piece of the integrand in the second term's integral above, since it goes as $\frac{1}{\beta H'} \to 0$ for small y, and $\beta H' e^{-\beta H'} \to 0$ for large y. Thus in the $\beta H' \to \infty$ limit, we now have a T-linear behaviour in the specific heat. This is also in order, because once the temperature becomes much smaller than the energy scale associated with the magnetic field, then the spinon occupations effectively correspond to a situation with a fermi surface, where a T-linear behaviour in the specific heat is expected. So, in the presence of the magnetic field, the specific heat interpolates between a T-linear behaviour as $\beta H' \to \infty$ to a T^2 behaviour as $\beta H' \to 0$. The coefficients in Eq. 14 are not considered sacrosanct when used as a fitting form for experimental data, since they were arrived at using several assumptions. But the T-dependence interpolation in presence of an applied field is taken seriously when using Dirac QSL ansatz for phenomenology.

Our theoretically calculated non spin-polarized total and Cu-d partial density of states (DOS) plot is shown below.

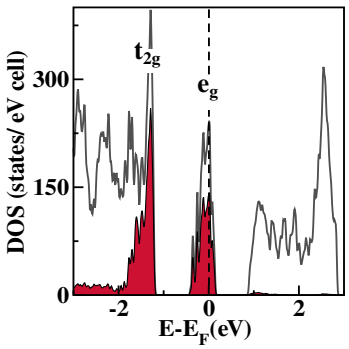

Figure 16: Non-spin polarized total (grey) and Cu-d partial (red) DOS for SCSO.

VIII. ELECTRONIC STRUCTURE CALCULATION

The electronic structure calculations were done for an ordered crystal structure, such that within the unit cell of $Sr_3CuSb_2O_9$, Cu atoms are connected through two consecutive Sb atoms forming a Cu-Cu triangular network within (111) plane. To construct such a crystal structure we have considered an ordered 3×3×3 super-cell (containing 270 atoms) of the two formula unit primitive unit cell of the parent compound $Sr(Cu,Sb)O_3$. The triangular Cu layers on the (111) plane are connected via Cu-O-Sb-O-Sb-O-Cu path. The distances between the six nearest neighbor Cu atoms in the triangular network are nearly identical. The local CuO_6 octahedral environment breaks the degeneracy of Cu-d orbitals into triply degenerate t_{2g} and doubly degenerate e_g orbitals.

* Electronic address: skundu37@gmail.com
† Electronic address: mahajan@phy.iitb.ac.in

[1] J. R. Carvajal, Abstracts of the Satellite Meeting on Powder Diffraction of the XV Congress of the IUCr (1990), unpublished.
[2] K. Momma and F. Izumi, J. Appl. Cryst. **44**, 1272 (2011).
[3] Y. Han, M. Hagiwara, T. Nakano, Y. Nozue, K. Kimura, M. Halim, and S. Nakatsuji, Phys. Rev. B **92**, 180410(R) (2015).
[4] K. Y. Zeng, L. Ma, Y. X. Gao, Z. M. Tian, L. S. Ling, and L. Pi, Phys. Rev. B **102**, 045149 (2020).
[5] Y. Li, D. Adroja, P. K. Biswas, P. J. Baker, Q. Zhang, J. Liu, A. A. Tsirlin, P. Gegenwart, and Q. Zhang, Phys. Rev. Lett. **117**, 097201 (2016).
[6] X.-G. Wen, *Quantum Field Theory of Many-Body Systems: From the Origin of Sound to an Origin of Light and Electrons* (Oxford University Press, 2007).

[7] Y. Iqbal, W.-J. Hu, R. Thomale, D. Poilblanc, and F. Becca, Phys. Rev. B **93**, 144411 (2016).
[8] We make the usual observation that changes in the chemical potential due to finite temperatures causes at most subleading order corrections.